SISSA

Calibration method and photon flux influences tiled flat-panel photon counting detector image uniformity in computed tomography

View the article online for updates and enhancements.

TECHNICAL REPORT

Calibration method and photon flux influences tiled flat-panel photon counting detector image uniformity in computed tomography

S.I. Inkinen,[a,1] **M.A.K. Juntunen,**[a,b,c] **A. Kotiaho**[a,b,c] **and M.T. Nieminen**[a,b,c]

[a]*Research Unit of Medical Imaging, Physics and Technology, University of Oulu,*
Aapistie 5A, FI-90220, Oulu, Finland

[b]*Medical Research Center, University of Oulu and Oulu University Hospital,*
Oulu, Aapistie 5A, FI-90220, Oulu, Finland

[c]*Department of Diagnostic Radiology, Oulu University Hospital,*
POB 50, FI-90029, Oulu, Finland

E-mail: satu.inkinen@oulu.fi

Abstract: The aim of this study is to compare how different calibration methods influence the image quality of photon-counting detector computed tomography (PCD-CT) at high and low photon fluxes. We investigate the performance of flat-field correction, signal-to-equivalent thickness calibration (STC), and polynomial correction (PC) methods using polymethyl methacrylate (PMMA) and iron as calibration materials. Two different cylindrical imaging phantoms containing contrast targets were scanned: an agar phantom and a phantom consisting of titanium hip implant embedded in agar. The scans were acquired using 120 kVp, and the energy thresholds of the PCD were set at 10 keV and 60 keV to obtain low energy (10–60 keV), high energy (60–120 keV) and total energy images (10–120 keV). Additionally, virtual monochromatic images (VMIs) with energies between 60–180 keV with 20 keV increments were generated from PC data. The reconstructions were made using filtered back projection, and image quality was assessed by evaluating image noise, contrast-to-noise ratio (CNR), and image uniformity. Overall, STC with PMMA as calibration material yielded the best image quality in terms of CNR and uniformity. Flat-field correction produced uniform reconstruction at low photon flux, but the performance degraded substantially at high flux. STC with iron as calibration material did not improve the reconstructions of the titanium hip implant. The beam hardening effects arising from metal were reduced when the VMI energy was increased while the CNR evaluated from agar phantom decreased with increasing energy of the VMI. Over the methods investigated, STC with PMMA was the most optimal calibration method for PCD-CT, yielding excellent image uniformity with both photon flux conditions.

Keywords: Computerized Tomography (CT) and Computed Radiography (CR); Data processing methods; Image reconstruction in medical imaging; X-ray detectors

---

[1]Corresponding author.

Contents

1 Introduction

Photon counting detectors (PCDs) and their applications in computed tomography (CT) are currently intensively studied [1–3]. PCDs convert the photon interaction in the conversion material into an electrical pulse whose height is proportional to the photon energy. Through pulse height discrimination, the PCD can differentiate the photon energies and distribute the photons into specific energy windows enabling spectral X-ray imaging [2]. PCDs are more advantageous to the conventional energy integrating detectors (EIDs) since, PCDs have higher detection efficiency, improved resolution, and reduced electronic and Swank noise compared to EIDs [2]. Furthermore, they open new possibilities for material characterization [4], K-edge imaging [5, 6], and multi-contrast agent imaging [7].

Despite the improvements of the PCDs over EIDs, there exist challenges such as, charge sharing, and pulse pile-up effects which substantially reduce the spectral discrimination power and detection

efficiency of PCDs [8, 9]. When a photon hits the detector conversion material, it interacts with the material itself, causing secondary effects such as K-escape and scattering degrading the energy resolution of the detector. Diffusion effects and Coulomb repulsion expands the charge cloud generated by the X-ray photon interaction, and consequently, the charge distribution might be registered in several adjacent pixels, degrading the energy resolution and spatial resolution of the detector [10]. In addition, loss of counts happens when quasicoincident photons arrive within a dead time and are registered as a one event. Dead time is the minimum required time period in order to record two events as separate pulses [11]. Quasicoincident photons cause pulse pile-up and distort the recorded energy. On the other hand, the pulse pile-up of quasicoincident photons can cause subthreshold events to be recorded as one instead of no events [9]. Especially at high photon fluxes, the pile-up effects increase.

The small pixel sizes with current PCDs result in prominent charge sharing effects. Therefore, charge sharing correction (CC) methods have been developed to mitigate these effects [9, 10]. As an example for CC, the counts from neighboring pixels occurring within a small time period can be summed and assigned to the pixel with the highest pulse height, restoring the energy level detected from the photon [9, 10]. However, CC methods increase the dead time of the PCD since they require further processing in the application-specific integrated circuit (ASIC) [12]. The high photon fluxes of clinical CT (~10^9 photons/mm^{2}s) [12], will, therefore, result in substantial count rate losses when PCDs are used.

Cadmium telluride (CdTe) and cadmium zinc telluride (Cd(Zn)Te) are the most promising direct converting semiconductor materials for medical CT applications [13]. Currently, flat-panel PCDs with large field-of-view are constructed from smaller submodules or tiles [14]. However, the tiled structure of PCDs is challenging, since the energy responses can vary between tiles and individual pixels, and the tile-borders can induce ringing artifacts [4, 15]. Pulse pile-up, charge sharing, nonuniform detector response to pulse amplification, and threshold inhomogeneity cause this variation [16]. Since the instability of the panel significantly deteriorates the reconstruction quality, the development of suitable calibration methods for correcting these effects is essential in order to mitigate tile- and pixel-wise variations.

Flat-field (FF) correction is commonly used for EIDs, and it has also been applied for PCDs [17, 18]. However, due to the non-linearity of detection efficiency with PCDs, a conventional FF correction scheme does not always sufficiently correct the attenuation effects such as beam hardening, especially in high photon flux conditions [16, 17]. For PCDs, another commonly used calibration approach is the signal-to-equivalent thickness calibration (STC) method that maps the measured count into calibration material thickness [19]. In this approach, the calibration material should have similar attenuation properties to the target tissues. Consequently, for soft tissues, PMMA is usually used as a calibration material because of its similar attenuation properties. In the case of a high atomic number material such as a metallic implant, STC correction may not work as expected, since neither PMMA nor metallic calibration material model the overall attenuation in a patient with a metal implant. However, this has not been previously studied. In our previous study [4], we briefly compared different calibration techniques such as FF correction, STC [19, 20], and polynomial calibration (PC) [21], and observed substantial differences between the methods in image quality, panel uniformity, and material decomposition accuracy.

This study aims to compare the impact of previously proposed calibration approaches [19, 21] on PCD-CT reconstruction image quality at low photon flux (negligible count rate losses and pulse

pile-up) and high photon flux (substantial count rate losses and pulse pile-up). Specifically, we will assess the influence of photon flux on the calibration performance. To our knowledge, the assessment on the effect of flux-conditions on the calibration performance has not been investigated in previous research. Furthermore, to analyze whether the performance of the calibration methods is affected by the target material, we will evaluate the image quality in a soft tissue-mimicking uniformity phantom made from agar, and in a soft-tissue phantom containing strongly attenuating high atomic number material, i.e., titanium hip implant.

2 Materials and methods

2.1 Phantom model

Two custom agar phantoms were constructed in cylindrical (diameter = 11 cm) PMMA containers. The first phantom was used in the evaluation of reconstruction field uniformity and served as a reference for image quality comparison. The second phantom contained a titanium hip prosthesis (Pinnacle Hip Solution, DePuy Synthes, MA, U.S.A.), and was used to investigate whether the performance of the calibration method differs for highly attenuating material. Both phantoms also contained contrast targets, i.e., standard solid tissue equivalent plugs of lung and bone (diam = 5 mm, length = 25 mm) from the anthropomorphic adult male phantom (ATOM 701-C, CIRS Inc., Norfolk, VA) (figure 1).

2.2 Photon counting detector

A large field-of-view (total active area of 51.3×154.7 mm^2, height $\times$ width) CdTe photon-counting detector (XC-Flite FX15, XCounter, Danderyd, Sweden) with two 12-bit counters was used. The PCD is constructed from 24 tiles, each tile having a 256×128-pixel area (height $\times$ width) with a 100 μm pixel pitch and a 100 μm gap between tiles. The adjustable energy thresholds were set to 10 keV and 60 keV. The 10 keV lower threshold was applied to remove electronic noise. During image acquisition, the PCD collects data into total energy (TE, 10–120 keV) and high energy (HE, 60–120 keV) images. The low energy (LE) images were obtained offline by computing LE = TE - HE.

2.3 Dead time analysis

To evaluate the dead time of the detector, separate dead time measurements were conducted. The lower threshold was kept at 10 keV, and analysis was performed in the TE image of one detector tile. An X-ray tube (XRB150PN600X4009, Spellman High Voltage Electronics Corporation, NY, U.S.A.) was used at 120 kVp in the characterization measurements. A tube current range of 0 to 4.395 mA was covered with 37 measurements. Two sets of measurements were conducted with and without a charge sharing correction, respectively. The dead time analysis was performed on one tile by fitting a paralyzable model [11]:

$$m = ne^{-\tau n}, \tag{2.1}$$

where m is the measured count rate from one tile as mean counts/s and n is the true count rate as counts/s estimated from the measurements by simply fitting a line to the first charge sharing correction off measurement (negligible count rate losses) with a tube current of 0.915 mA. Subsequently,

the tube current used in the measurements was mapped into true counts using the slope value. For the paralyzable model, nonlinear fitting using a Nelder-Mead simplex algorithm was performed, and the dead time was estimated. Finally, the low and high photon flux tomography measurement conditions were visualized to demonstrate the extent of pile-up in the PCD-CT measurements.
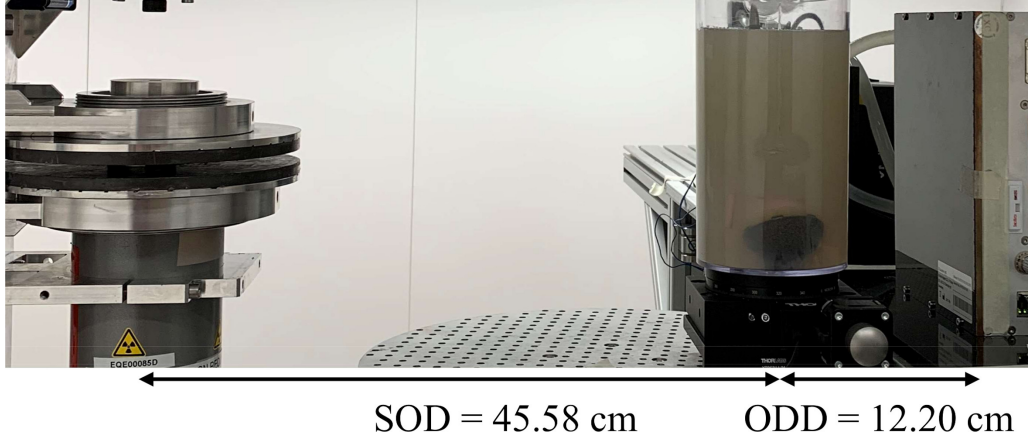

SOD = 45.58 cm   ODD = 12.20 cm

Figure 1. Image of the PCD-CT imaging set-up marked with source-to-object distance (SOD) and object-to-detector distance (ODD). Agar phantom with titanium hip implant and contrast targets is on top of a motorized rotator.

2.4   Photon counting computed tomography

The phantom was positioned on a motorized rotational stage (NR360S/M, Thorlabs, Inc., Newton, New Jersey, U.S.A.), and the rotation axis was fixed to the center of the PCD's active area using a laser designator (figure 1). The tube voltage of the X-ray tube (MXRP-160, COMET Group, Flamatt, Switzerland) was set to 120 kVp, and the tube current was set to 1 mA and 8 mA for low and high photon flux measurements, respectively. The average ratios for the number of counts in the air scans were HE/TE = 0.4 and LE/TE = 0.6 for both photon flux conditions. The effective focal spot of the X-ray tube was 0.4 mm × 4 mm (height × width, EN12543 standard), and the X-ray tube had tungsten anode with an inherent filtration of 0.5 mm Ti + 2.0 mm H_2O + 2.0 mm Al. The vertical collimation of the X-ray tube was set to 4.88 cm at the detector. The source-to-detector distance was 57.78 cm, and to reduce magnification, the motorized rotator was set as close as possible (12.20 cm) to the detector. The angular velocity of the motorized rotation stage was set at 4 °/s and 16 °/s for low and high photon flux measurements, respectively. The total scan times were 90 s and 22.5 s. The frame rate for image acquisition was set to 40 Hz and 64 Hz, for low and high photon flux tomography measurements, respectively. 10 and 2 consecutive frames were averaged to obtain one projection per degree with a total exposure of 90 mAs for both flux measurements. Charge sharing correction was used during acquisition to reduce charge dispersion at the detector in the tomography measurements. No anti-scatter grid was used.
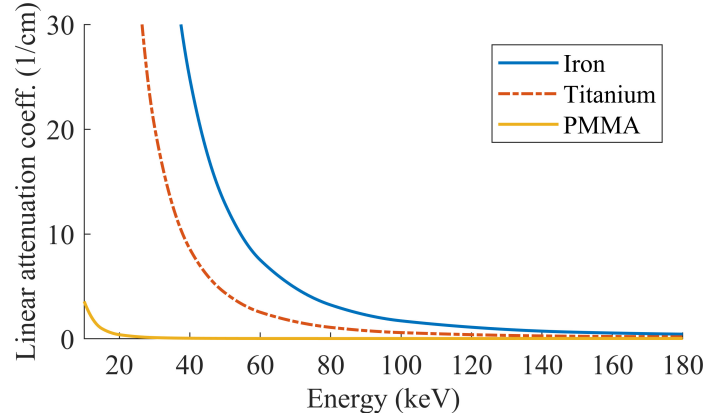
Figure 2. Linear attenuation coefficients for the used calibration materials (PMMA, iron), and titanium. The linear attenuation coefficient of titanium is between those of the used calibration materials and it can thus be represented as a linear combination of attenuation coefficients of iron and PMMA. Linear attenuation coefficients transformed from NIST database mass attenuation coefficients [22].

2.5 Image processing in the projection domain

2.5.1 Pre-processing

Prior to calibration, the 100 μm gaps between tiles were interpolated using mean filtering from adjacent pixel values. Subsequently, the projection data was resized to match the reconstruction voxel size of a typical clinical musculoskeletal CT scan of 0.23 mm × 0.23 mm × 0.6 mm. To limit our study on the performance of the calibration methods at high photon flux, no dead time pre-correction was performed for the acquired raw data.

2.5.2 Calibration techniques

Projection data were corrected using the conventional flat-field correction (FF), signal-to-equivalent thickness calibration (STC), and polynomial calibration (PC) methods. For calibration, different thicknesses of PMMA {0, 3, 5.3, 7.3, 9.3, 10.7, 12.7 cm} and iron {0, 0.1, 0.2, 0.3, 0.5, 0.7, 1 cm} plates and their combinations {iron: 0.1, 0.2, 0.3, 0.5 cm; PMMA: 3, 5.3, 7.3, 10.7 cm} were measured. PMMA has similar attenuation properties to soft tissues, and it is, therefore, commonly used as calibration material. Iron was selected since it has a higher atomic number as compared to titanium, and a linear combination of PMMA and iron in PC could model the attenuation of titanium in PC (figure 2). The thicknesses for PMMA were selected to cover the attenuation range of the uniformity phantom. The iron thicknesses were selected to cover the measured count range encountered with the titanium implant. All subsequent analyses were conducted using MATLAB (v.9.4, The MathWorks Inc., Natick, MA, U.S.A.).

2.5.3 Flat-field correction (FF)

The measured counts (I_k) were FF-corrected for each energy window (LE, HE, and TE) with

$$I_k^{FF} = \frac{I_k}{I_{k0}}, \tag{2.2}$$

where k denotes energy window ($k = LE, HE, TE$), and I_{k0} is the air scan of the corresponding energy window. Subscript k indicates that the calibration is performed separately for each energy window.

2.5.4 Signal-to-equivalent thickness calibration (STC)

With the signal-to-equivalent thickness calibration (STC), the calibration is performed with different thicknesses of one calibration material [20]. The calibrations for both PMMA and iron were performed separately to evaluate how these materials estimate the attenuation of the metallic implant and the attenuation of the agar phantom. In STC, a following exponential attenuation model was fitted for each energy window k as:

$$I_k (A_k) = B_k e^{a_k A_k}, \tag{2.3}$$

where B_k and a_k are fitting parameters obtained pixel-wise from calibration measurements, and A_k is the calibration material thickness for each energy window ($k = LE, HE, TE$) (figure 3). Finally, the measured counts I_k were transformed into equivalent thicknesses (A_k) with

$$A_k = \frac{1}{a_k} \ln \left(\frac{I_k}{B_k} \right). \tag{2.4}$$

2.5.5 Polynomial calibration (PC)

Polynomial correction (PC) is an empirical material decomposition method in the projection domain [21]. In this study, PC was applied to decompose the LE and HE energy projections into projected iron and PMMA thicknesses (figure 4). In this method, the logarithm transformed FF-corrected images ($L_k = -\ln \left(I_k^{FF} \right)$) are mapped to projected thicknesses (A) using:

$$\begin{aligned} A^{\text{PMMA}} &= c_0 + c_1 L_{LE} + c_2 L_{HE} + c_3 L_{LE}^2 + c_4 L_{LE} L_{HE} + c_5 L_{HE}^2 \\ A^{\text{iron}} &= d_0 + d_1 L_{LE} + d_2 L_{HE} + d_3 L_{LE}^2 + d_4 L_{LE} L_{HE} + d_5 L_{HE}^2 . \end{aligned} \tag{2.5}$$

Calibration parameters for iron and PMMA (c_i, d_i, $i = 0, 1, \ldots, 5$) were obtained for each pixel (figure 4).

2.5.6 Virtual monochromatic energy projections

The projected thickness images decomposed with PC (A^{PMMA}, and A^{iron}) were used to obtain the virtual monochromatic image (VMI) projections (p_E) as

$$p_E = \mu_E^{\text{PMMA}} A^{\text{PMMA}} + \mu_E^{\text{iron}} A^{\text{iron}}, \tag{2.6}$$

where μ_E is the linear attenuation coefficient of the decomposed basis material at selected mono-energy (E). Linear attenuation coefficients were calculated by multiplying the known density of the calibration materials with their mass attenuation coefficients obtained from the NIST database [22]. The selected virtual mono-energies were {60, 80, 100, 120, 140, 180} keV.
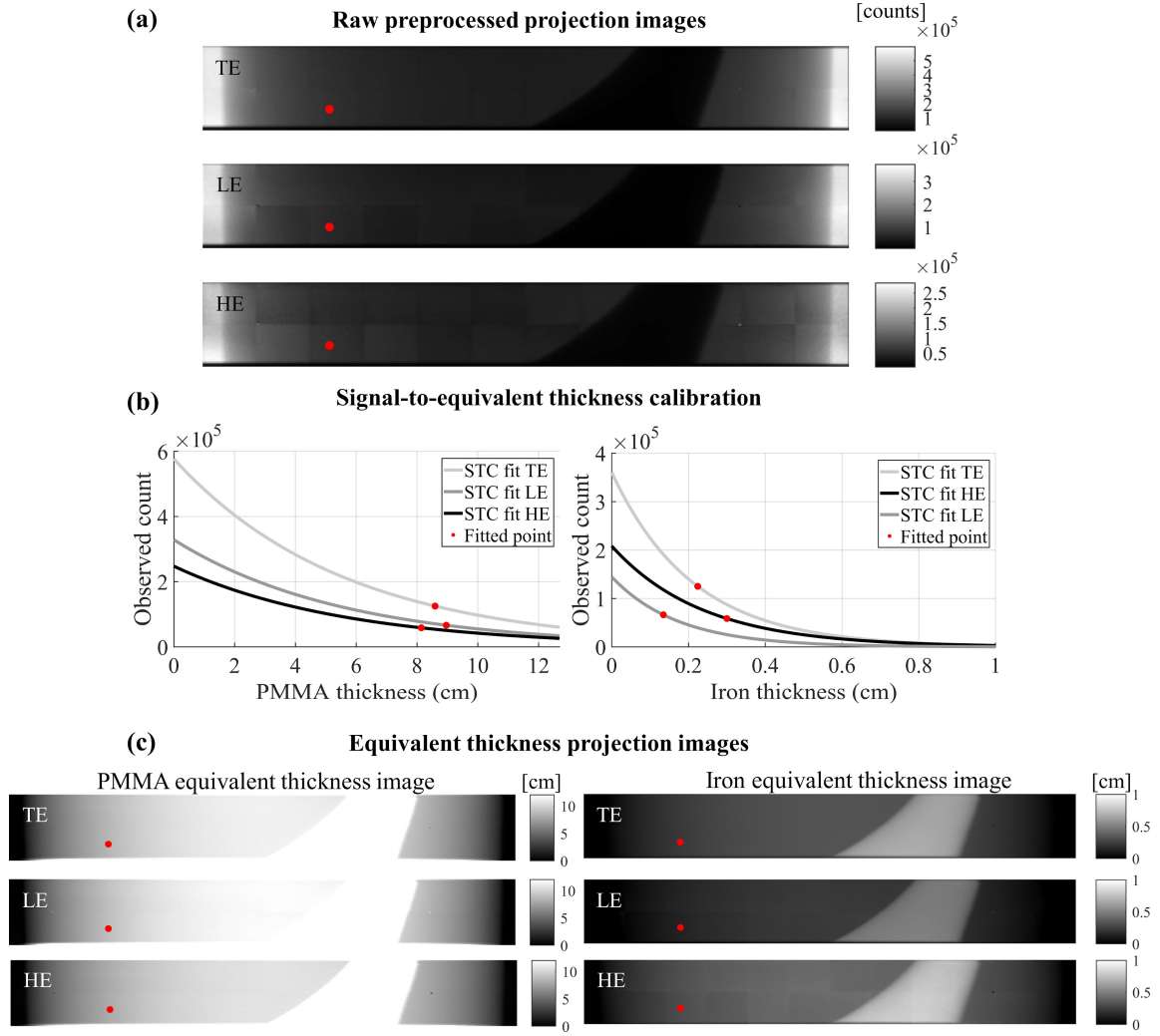
Figure 3. Illustration of the signal-to-equivalent thickness correction for PMMA and iron for one detector pixel (marked as red dot). (a) Raw preprocessed photon count images over all energy windows. (b) Signal-to-equivalent thickness calibration curves for PMMA and iron in which the thickness was estimated using equation (2.4). Fit was estimated for each detector pixel separately. (c) Calibrated equivalent thickness projection images.

2.5.7 Reconstruction

Conventional filtered back projection (FBP) reconstruction method was used to evaluate the uniformity of the field of view and the metal artifacts present in the reconstructions of different calibration methods and photon flux conditions. Projections for each energy window (LE, HE, TE) and VMI projections were reconstructed. A custom FBP filter with Hann windowing and 6-pixel moving average filter was used for all measurements. All slices were reconstructed in 2D with the fan beam geometry using ASTRA (Vision Lab, University of Antwerp, Belgium) [23] and Spot (v.1.2) toolboxes [24]. After reconstruction, image stacks were transformed into Hounsfield Units (HUs) by approximating the voxel value of agar to be the same as water.
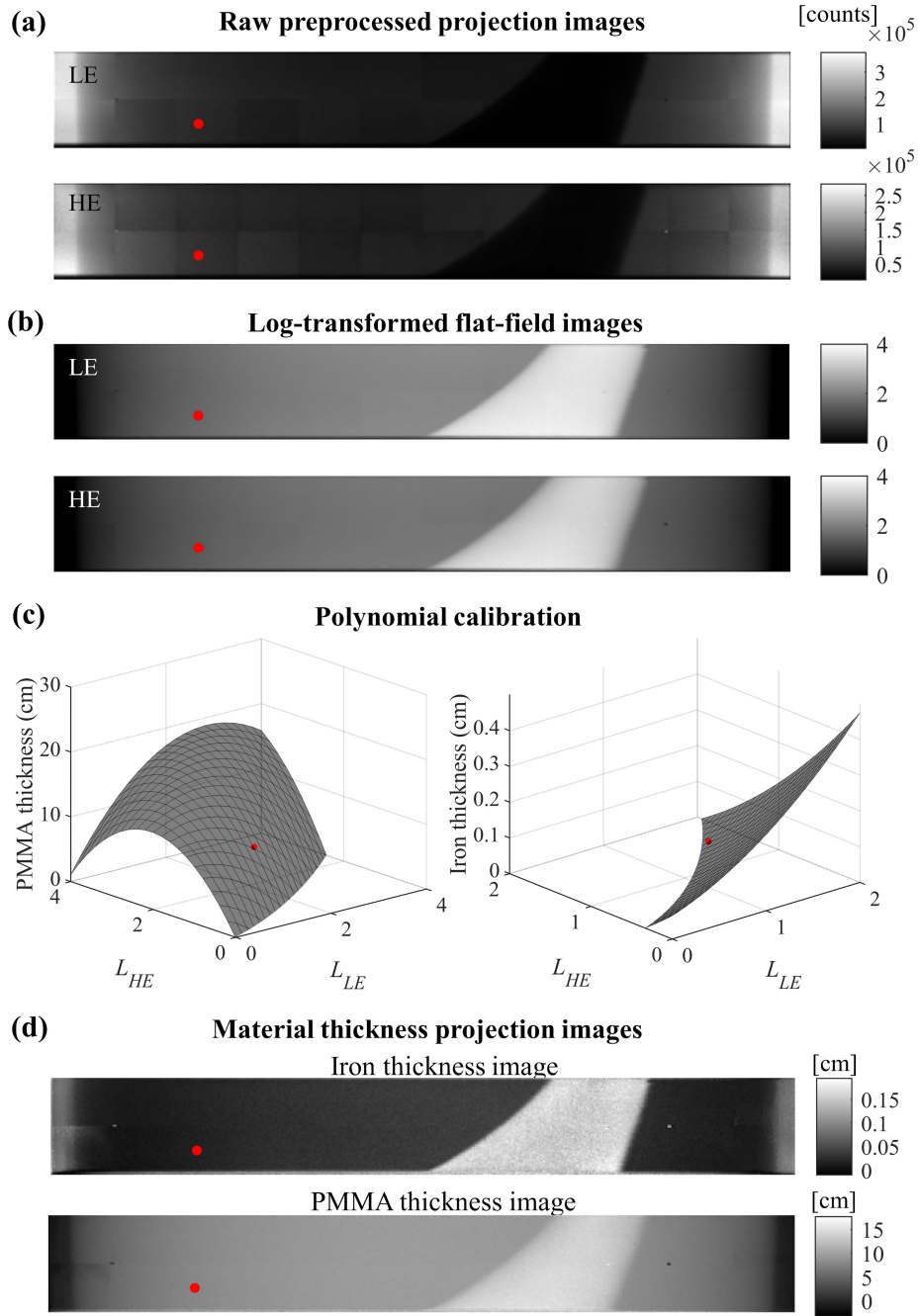
Figure 4. Illustration of the polynomial calibration for one detector pixel (marked as red dot). Fit was estimated for each detector pixel separately. (a) Raw preprocessed photon count images over LE and HE energy windows. (b) Logarithm transformed flat-field images which are used as input for (c) polynomial calibration which produces (d) material decomposed PMMA and iron thickness images.

2.5.8 Assessment of image uniformity, contrast-to-noise ratio, and noise

For the evaluation of image uniformity, i.e., the extent of ringing and cupping artifacts, a circular mask was placed into the center of the agar image slice (figure 5 a)), and the standard deviation

(SD) was determined from that region. For image quality assessment, two descriptive parameters were selected: 1) standard deviation (SD) of the background (figure 5 b)), diameter = 50 pixels) to evaluate the severity of streaking artifacts, and 2) contrast-to-noise ratio (CNR) of bone (figure 5 c)) and lung (figure 5 d)) contrast targets. The location for the estimation of streaking artifacts was fixed near to the edge of the phantom in order to account only for the streaking and to exclude the photon starvation artifacts near the metallic implant. For CNR, the region of interest (ROI) was manually placed as a circular mask (diameter = 14 pixels) for each contrast target, as shown in figure 5 c)-d) (blue annotations), and background was evaluated using an ROI surrounding the target (figure 5 c)-d), red annotations). The mean HU of the target and background ROIs were determined and subtracted, and then divided with the standard deviation of the background ROI to obtain the CNR. All parameters were evaluated for 5 subsequent slices, and mean ± standard deviation was visualized to determine the performance over the whole phantom.
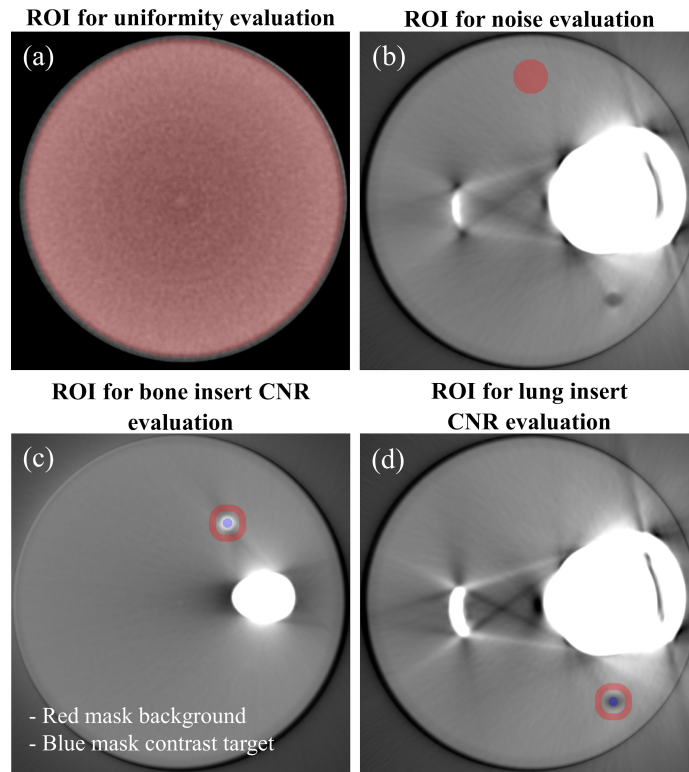

Figure 5. Illustration of the region of interest (ROI) in the assessment of image uniformity, contrast-to- noise ratio, and noise from agar phantoms (see section 2.1). (a) ROI for the evaluation of image uniformity, (b) ROI for evaluation of image noise, ROIs for (a) bone and (d) lung inserts for contrast-to noise-ratio evaluation.

3 Results

Hereafter, the calibration method and material are notated with the identifier: calibration method$_{Material}$ (e.g., STC$_{PMMA}$).
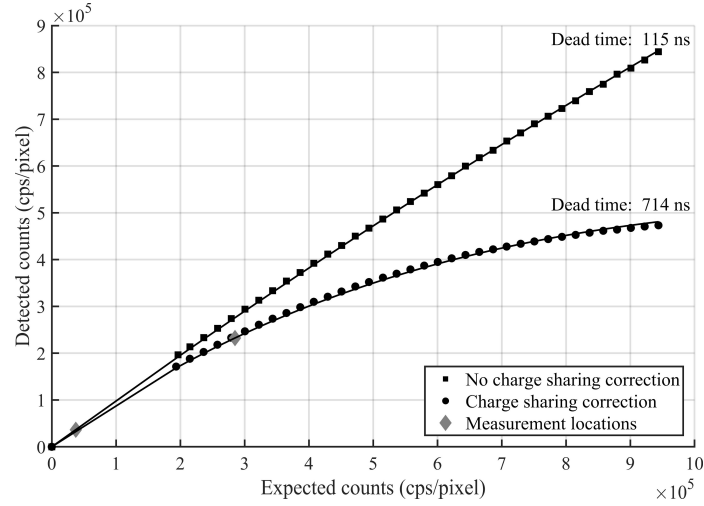
Figure 6. Characterization of PCD dead time with and without charge sharing correction. The photon fluxes for high and low photon flux PCD-CT measurements are marked as diamonds.

3.1   Dead time analysis

The measured dead times for the detector were 714 ns and 115 ns with and without charge sharing correction, respectively (figure 6). The low photon flux tomography measurement was in the region with negligible count rate losses, whereas the high photon flux measurement was in the region of substantial count rate loss.
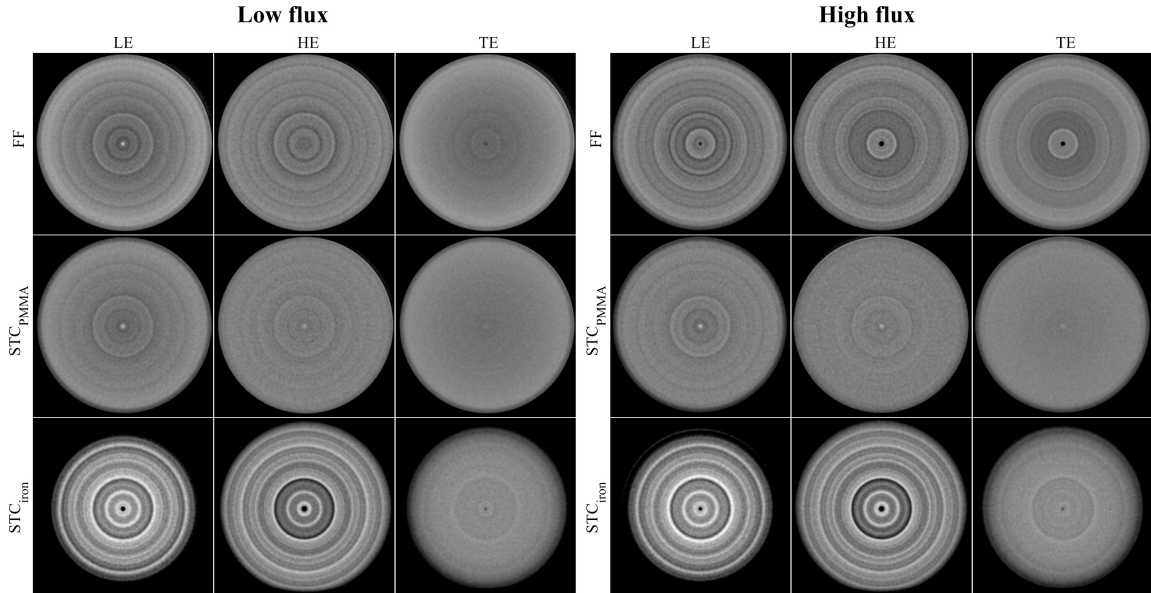

Figure 7. Low and high flux reconstructions of the uniformity phantom. The STC$_{PMMA}$ correction yielded the most uniform response with the least cupping present. The ringing is most pronounced in STC$_{Iron}$ correction. The windowing is set to [-250, 250] HU.

Table 1. Uniformity results presented as standard deviation (SD).

Calibration material	Energy	Method	Low flux SD (HU)	High flux SD (HU)
	LE	FF	35.3	29.7
	HE	FF	19.4	27.4
	TE	FF	30.1	27.7
PMMA	LE	STC	22.3	23.2
PMMA	HE	STC	11.0	12.5
PMMA	TE	STC	17.5	16.4
Iron	LE	STC	329.5	290.8
Iron	HE	STC	55.0	56.1
Iron	TE	STC	145.3	130.5
PMMA & Iron	60 keV	PC	56.2	70.9
PMMA & Iron	80 keV	PC	33.7	35.6
PMMA & Iron	100 keV	PC	43.8	41.6
PMMA & Iron	120 keV	PC	47.1	43.5
PMMA & Iron	140 keV	PC	51.4	46.4
PMMA & Iron	180 keV	PC	55.3	49.9

3.2 Reconstruction uniformity with different photon flux conditions

STC_{PMMA} calibration produced the highest image uniformity over other calibration methods in both low and high photon flux conditions showing the least ringing artifacts from the tile gaps, sensitivity differences between tiles and least cupping (figures 7 and 8, table 1). The increased photon flux did not substantially influence the image uniformity with STC_{PMMA}. The performance of FF correction, on the other hand, decreased with increased flux resulting in notable ringing. When using iron i.e., high-Z calibration material in the calibration, the detector tiles were least uniform for both flux conditions.

The PC enabled the generation of virtual monochromatic images, and the cupping increased when the energy was increased (figure 8), manifesting as decreased image uniformity (table 1). The performance of VMIs was similar in low and high photon flux conditions.

3.3 Metal artifacts for different calibration methods and flux conditions

Metal artifacts were present in each image, and the use of iron as calibration material did not yield any improvements in the STC method (figure 9). The reconstructions from FF and STC_{Iron} correction showed ringing in regions with no metal in LE and HE images (figure 9). The STC_{PMMA} corrected reconstruction had the visually most uniform image. When compared over energy channels, both HE and TE images had the best image quality (figures 9 and 11).
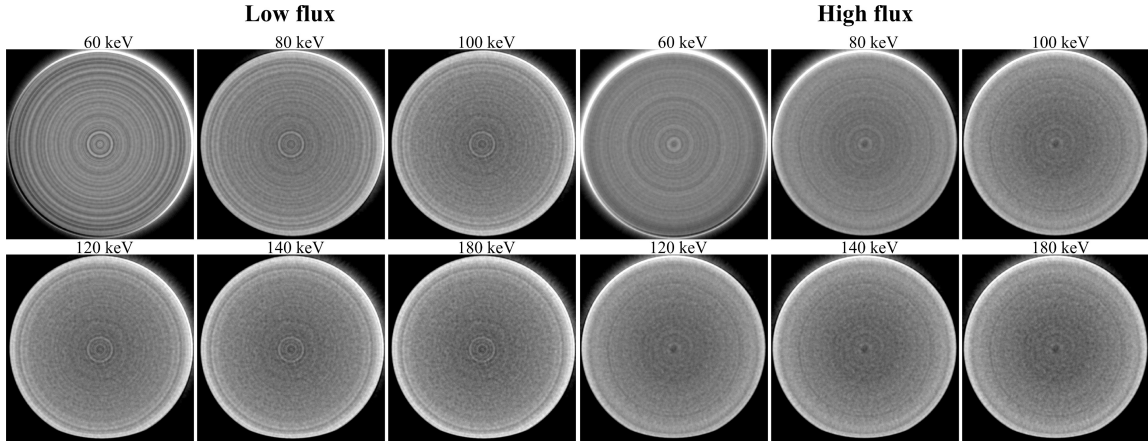
Figure 8. Uniformity images over increasing virtual monochromatic photon energies. At low keV the ringing is more prominent and diminishes when the VMI increases. In turn the cupping increases. The windowing is set to [-250, 250] HU.
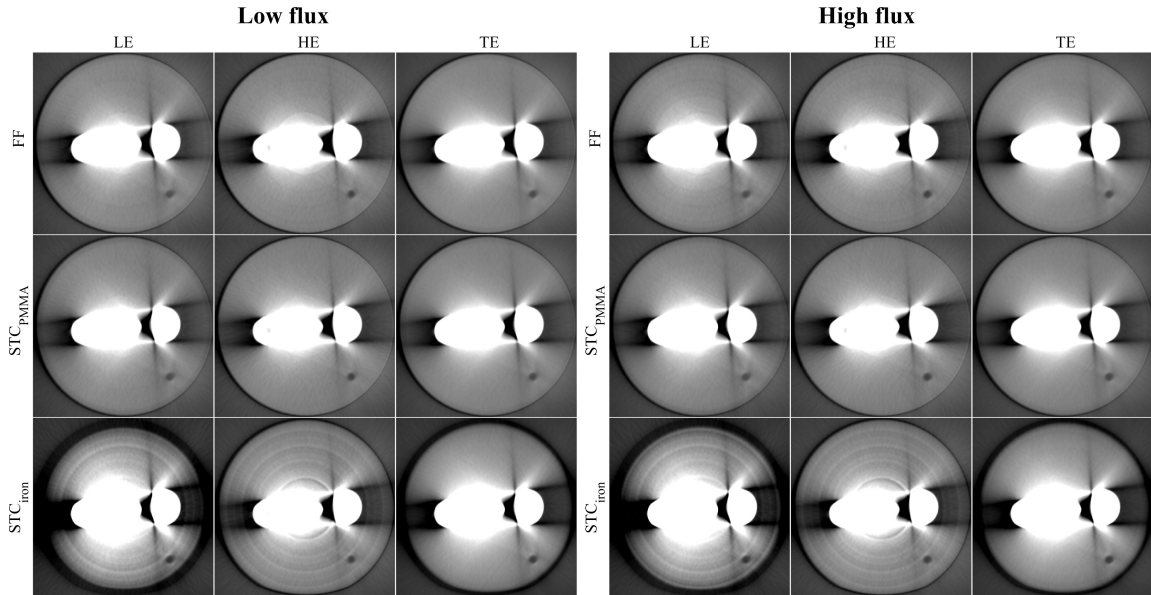

Figure 9. The titanium hip implant reconstructions for different calibration methods and photon flux conditions. The best image quality is observed with STC$_{PMMA}$ calibration. The windowing is set to [- 1000, 1000] HU.

For VMIs, the photon starvation artifact was decreased with increasing mono-energy (figure 10). However, the noise was increased with increasing mono-energy (figure 11). The performance was similar for VMIs at low and high photon flux conditions. Consequently, as noise increased and contrast decreased with increasing energy, CNR also decreased (figure 11). Finally, the VMIs exhibited ringing that originated from the metal implant at low photon flux (figure 10), whereas this ringing was less evident in the soft tissue region of the phantom.

When comparing technical image quality parameters, the STC$_{PMMA}$ provided the best image quality with the highest CNR over all methods (figure 11). However, the blooming artifacts arising from the metal implant were only reduced with the high energy VMIs.
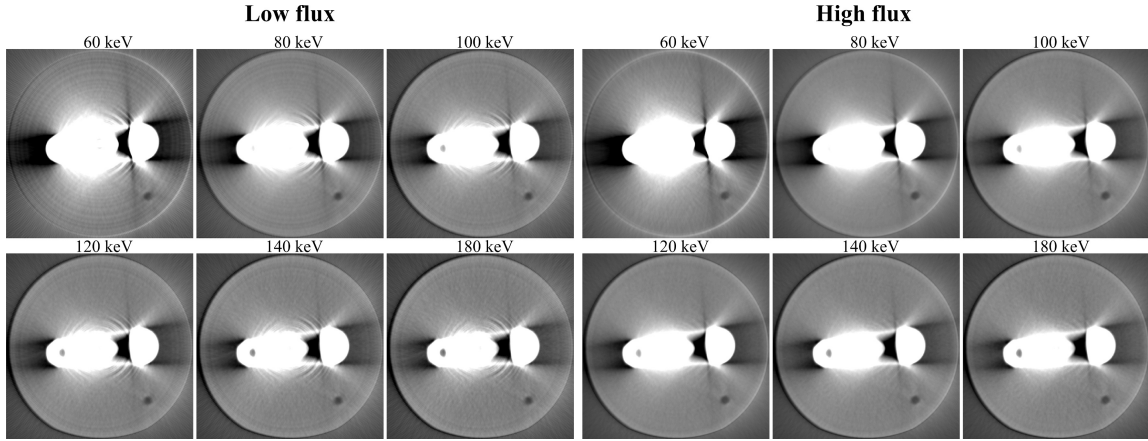
Figure 10. Virtual monochromatic images from titanium hip implant phantom. The windowing is set to [-1000, 1000] HU.

4   Discussion

This study compared how different calibration methods affect the reconstruction quality for flat-panel PCD-CT at different photon flux and attenuation conditions. Flat-field correction, signal-to-equivalent thickness calibration, and polynomial correction methods were selected since they are commonly used for PCDs. The overall best performance was found with STC with PMMA as the calibration material at both low and high photon flux conditions. However, the blooming and photon starvation artifacts arising from the metal implant were suppressed with high energy VMIs obtained using PC.

In low photon flux conditions (negligible count rate losses), FF correction resulted in sufficient image quality. In high photon flux conditions, however, the STC_{PMMA} method yielded substantially better results over FF correction that portrayed visible tile-to-tile variations. These variations likely resulted from the count rate losses in the air scan: during object scanning, the photon flux is reduced due to X-ray attenuation within the object and, therefore, count rate losses and the transmitted X-ray spectra deviate between flat-field and object scans. This reasoning is consistent also with the outcomes of [4, 16], where FF performed poorly in terms of inter-tile variation. The STC method approximates the exponential attenuation of the reduced photon flux at the detector through thickness-based calibration. Therefore, it provided better calibration performance and a more experimentally grounded approach for high photon flux scenarios [4, 16].

The STC method is often used for PCD calibration since it accounts for the detection efficiency and energy dependence of each pixel individually [20]. The calibration material for STC should have similar attenuation properties to the object to be imaged, e.g., PMMA for soft tissues [20]. In this study, we found that PMMA is also suitable when there is a mixture of low atomic number (Z) and high-Z material present, as was the case in the titanium hip implant phantom. High-Z calibration material, such as iron, on the other hand, generated tile non-uniformities in the soft tissue regions, which manifested as ringing artifacts in the reconstructed images, and no improvement was observed with the titanium hip implant phantom.
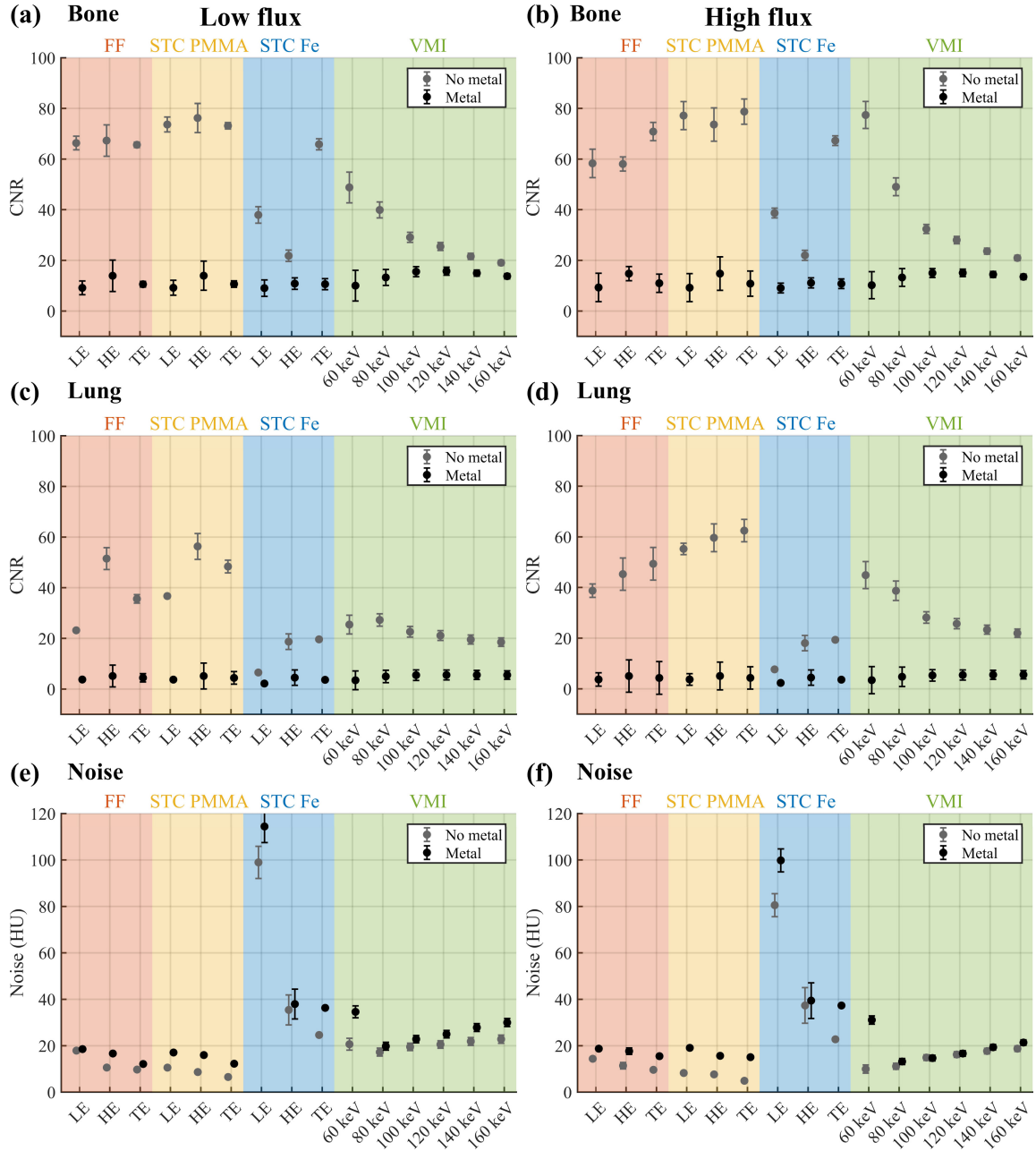
Figure 11. Image quality comparison (Mean ± standard deviation, N=5) of different energy window reconstructions made from calibrated projection data using flat-field (FF) correction, signal-to-equivalent thickness calibration (STC) with PMMA and iron and virtual monochromatic images (VMIs) made using polynomial correction. CNR for bone (a) at low photon flux, (b) at high photon flux and lung contrast targets (c) at low photon flux and (d) high photon flux, and noise at (e) low photon flux and (f) high photon flux.

The PC for dual-material calibration was included to study whether combining both iron and PMMA in calibration could provide a more robust calibration framework. As two-counter PCD allows spectral differentiation to LE and HE images, two-material calibration can be performed with PC. The virtual monochromatic images were determined from these dual-material calibrated

projections, which have not been investigated for metal artifacts in prior PCD-CT studies. We observed that dual-material calibration had slightly inferior performance compared to STC_{PMMA}. Moreover, increasing the virtual monochromatic energy reduced beam hardening effects arising from the metal implant, which is consistent with previous research with dual-energy CT [25, 26]. The improvements were minor when the virtual monochromatic energy was over 120 keV, since increasing the virtual monochromatic energy from 120 keV to 180 keV produced only a minute reduction of BH artifacts. This was expected since the linear attenuation coefficients of iron and PMMA vary only slightly at such high energies. In turn, CNR was reduced for increasing virtual monochromatic energy, which has also been reported for DECT [26]. In addition, virtual monoenergetic imaging through spectral CT has been demonstrated as an effective tool for improving HU number stability [27]. In the present study, however, VMIs did not produce substantial improvements in HU number stability compared to STC. We believe that thickness-based calibration in STC provides effective correction for beam hardening and scattering, and therefore, VMIs did not yield any further improvements in uniformity.

In this study, three energy windows (LE (10–60 keV), HE (60–120 keV), and TE (10–120 keV)) were used. Rajendran et al. 2014 reported that beam hardening and streaking artifacts resulted in deteriorated overall image quality in TE window when compared to HE window image. We observed that CNR was improved in HE window images at low photon flux conditions, but at high photon flux, the best performance was with both TE and HE. However, the number of photons in different energy windows has a substantial impact on the perceived image quality. As the TE window contains all photons i.e., more than LE and HE windows, it also contains the least noise. Furthermore, the selection of the energy thresholds has a substantial impact on the photon statistics in LE and HE windows. Consequently, these aspects have to be taken into account when making direct image quality assessment between different energy windows.

Some limitations of our study need to be addressed. For the detector characterization, we applied a paralyzable model since it fitted better to our measurements, yet the actual detector behavior is between paralyzable and non-paralyzable models [28]. Furthermore, we observed tile- and pixel-wise variations in the dead time of the detector (data not shown). The reported dead time is an average of one tile to describe the overall characteristics of the PCD. An anti-scatter grid for the PCD was not used, which would likely have improved the image quality. Beam hardening effects could have been greatly reduced, especially in the HE images, if the peak kilovoltage had been increased, as demonstrated previously [3]. However, the X-ray tube peak kilovoltage of 120 kV was selected based on the commonly used musculoskeletal CT imaging protocol for titanium hip implants [29, 30]. The X-ray tube had an elongated and large focal spot, which might have an effect on the projection image quality causing penumbra effects. However, the imaging targets were placed as close to the detector as possible to mitigate this.

Even though the high photon flux condition showed count rate losses in the air scan, the imaging target attenuates photons reducing the extent of count rate loss at the detector. Non-iterative FBP reconstruction algorithm was chosen since it does not use regularization schemes for noise reduction. A more dedicated spectral reconstruction algorithm or more sophisticated iterative methods with regularization would probably have improved the image quality [31]. However, the aim of this study was to investigate the impact of photon flux on the performance of different PCD calibration approaches — not the impact of different reconstruction methods.

In future studies, the effect of dead time pre-correction in image quality should be investigated. Especially for flat-field correction, it could yield improvements in the high photon flux conditions with substantial count loss. In addition, the influence of calibration methods at the clinical photon flux ranges should be investigated because the high dead time of the PCD panels has been a significant limiting factor for their integration into clinical CT systems.

5 Conclusion

In this study, the impact of different calibration methods on PCD-CT reconstruction at different photon fluxes and attenuation conditions was investigated. The conventional flat-field correction yielded a sufficient image quality at low photon flux, whereas detector tile nonuniformities induced ringing artifacts at high photon flux. For the signal-to-equivalent thickness calibration method, the chosen calibration material had a substantial effect on the performance, and the best performing method was the signal-to-equivalent thickness calibration with PMMA as calibration material. The STC correction improved the tile- and reconstruction uniformity substantially at high photon fluxes when compared to FF correction. Finally, an increase in the energy of the virtual monochromatic images, obtained with the PC method, reduced beam hardening effects from the metal implant.

Acknowledgments

References

[1] P.M. Shikhaliev, T. Xu and S. Molloi, *Photon counting computed tomography: concept and initial results*, *Med. Phys.* **32** (2005) 427.

[2] K. Taguchi and J.S. Iwanczyk, *Vision* 20/20: *single photon counting X-ray detectors in medical imaging*, *Med. Phys.* **40** (2013) 100901.

[3] W. Zhou et al., *Reduction of metal artifacts and improvement in dose efficiency using photon-counting detector computed tomography and tin filtration*, *Invest. Radiol.* **54** (2019) 204.

[4] M.A.K. Juntunen et al., *Framework for photon counting quantitative material decomposition*, *IEEE Trans. Med. Imag.* **39** (2020) 35.

[5] E. Roessl, B. Brendel, J.-P. Schlomka, A. Thran and R. Proksa, *Sensitivity of photon-counting K-edge imaging: dependence on atomic number and object size*, *IEEE Nucl. Sci. Symp. Conf. Rec.* (2008) 4016.

[6] J.P. Schlomka et al., *Experimental feasibility of multi-energy photon-counting K-edge imaging in pre-clinical computed tomography*, *Phys. Med. Biol.* **53** (2008) 4031.

[7] R. Symons et al., *Dual-contrast agent photon-counting computed tomography of the heart: initial experience*, *Int. J. Cardiovasc. Imag.* **33** (2017) 1253.

[8] K. Taguchi et al., *Modeling the performance of a photon counting X-ray detector for CT: energy response and pulse pileup effects*, *Med. Phys.* **38** (2011) 1089.

[9] A.S. Wang, D. Harrison, V. Lobastov and J.E. Tkaczyk, *Pulse pileup statistics for energy discriminating photon counting X-ray detectors*, *Med. Phys.* **38** (2011) 4265.

[10] C. Ullberg, M. Urech, N. Weber, A. Engman, A. Redz and F. Henckel, *Measurements of a dual-energy fast photon counting CdTe detector with integrated charge sharing correction*, *Proc. SPIE* **8668** (2013) 86680P.

[11] G.F. Knoll, *Radiation detection and measurement*, (2005).

[12] M. Overdick et al., *Towards direct conversion detectors for medical imaging with X-rays*, *IEEE Nucl. Sci. Symp. Conf. Rec.* (2008) 1527.

[13] T. Schulman, *Si, CdTe and CdZnTe radiation detectors for imaging applications*, doctorate dissertation, University of Helsinki, Helsinki, Finland (2006).

[14] S. Leng et al., *Photon-counting detector CT: system design and clinical applications of an emerging technology*, *RadioGraphics* **39** (2019) 729.

[15] M. Ahmad et al., *First in-vivo experiments with a large field-of-view flat panel photon-counting detector*, in *Proc. 4*[th] *Intl. Mtg. image Form. X-ray CT*, (2016), pg. 105.

[16] M. Ahmad et al., *Assessment of a photon-counting detector for a dual-energy C-arm angiographic system*, *Med. Phys.* **44** (2017) 5938.

[17] D. Kim and J. Baek, *Comparison of flat field correction methods for photon-counting spectral CT images*, *IEEE Nucl. Sci. Symp. Med. Imag. Conf. Rec.* (2018) 1.

[18] H.-M. Cho, H.-J. Kim, Y.-N. Choi, S.-W. Lee, H.-J. Ryu and Y.-J. Lee, *The effects of photon flux on energy spectra and imaging characteristics in a photon-counting X-ray detector*, *Phys. Med. Biol.* **58** (2013) 4865.

[19] D. Vavrik, T. Holy, J. Jakubek, S. Pospisil, Z. Vykydal and J. Dammer, *Direct thickness calibration: way to radiographic study of soft tissues*, in *Astroparticle, particle and space physics, detectors and medical physics applications*, World Scientific, Singapore (2006), pg. 773.

[20] J. Jakubek, *Data processing and image reconstruction methods for pixel detectors*, *Nucl. Instrum. Meth. A* **576** (2007) 223.

[21] R.E. Alvarez, *Estimator for photon counting energy selective X-ray imaging with multibin pulse height analysis*, *Med. Phys.* **38** (2011) 2324.

[22] J.H. Hubbell and S.M. Seltzer, *X-ray mass attenuation coefficients*, *NIST Stand. Ref. Database* **126**, (2004).

[23] W. van Aarle et al., *Fast and flexible X-ray tomography using the ASTRA toolbox*, *Opt. Express* **24** (2016) 25129.

[24] E. van den Berg and M.P. Friedlander, *Spot — a linear-operator toolbox*, http://www.cs.ubc.ca/labs/scl/spot/, 7 August 2019.

[25] E. Pessis et al., *Virtual monochromatic spectral imaging with fast kilovoltage switching: reduction of metal artifacts at CT*, *RadioGraphics* **33** (2013) 573.

[26] R. Wellenberg et al., *Quantifying metal artefact reduction using virtual monochromatic dual-layer detector spectral CT imaging in unilateral and bilateral total hip prostheses*, *Eur. J. Radiol.* **88** (2017) 61.

[27] G. Michalak et al., *Technical note: improved CT number stability across patient size using dual-energy CT virtual monoenergetic imaging*, *Med. Phys.* **43** (2016) 513.

[28] J. Cammin, S. Kappler, T. Weidinger and K. Taguchi, *Evaluation of models of spectral distortions in photon-counting detectors for computed tomography*, *J. Med. Imaging* **3** (2016) 023503 [*Erratum ibid.* **3** (2016) 029801].

[29] M.-J. Lee et al., *Overcoming artifacts from metallic orthopedic implants at high-field-strength MR imaging and multi-detector CT*, *RadioGraphics* **27** (2007) 791.

[30] A. Blum et al., *CT of hip prosthesis: new techniques and new paradigms*, *Diagn. Interv. Imaging* **97** (2016) 725.

[31] R.A. Nasirudin et al., *Reduction of metal artifact in single photon-counting computed tomography by spectral-driven iterative reconstruction technique*, *PLoS One* **10** (2015) e0124831.